Research paper

Station-keeping for a solar sail during lander/probe deployment using feedback control

Iain Moore [*], Matteo Ceriotti, Colin R. McInnes

James Watt School of Engineering, University of Glasgow, University Avenue, Glasgow, G12 8QQ, Scotland, UK

ARTICLE INFO

ABSTRACT

Due to its propellantless nature, a solar sail can provide the primary propulsion system for a high energy mission, such as that of a multiple asteroid rendezvous. Upon arrival at an asteroid, it is often desirable to interact with the surface of the body, such as for sample extraction. The deployment of a lander from a solar sail carries the difficulty of an instantaneous, and sometimes considerable, change to the system dynamics at the point of separation. This paper investigates the effects of changing sail performance during the release of multiple "ChipSat" probes as well as a large MASCOT-type lander and the control of the sail into a positional hold at an equilibrium point or periodic orbit. In one scenario, 20 ChipSat probes are released, with one-hour spacing between each release. The sail is then controlled to maintain the sailcraft close to the initial deployment point. The performance of a Linear Quadratic Regulator (LQR) is compared with maintaining a fixed sail attitude after deployment. In a second scenario, at the point of separation of the larger MASCOT-type lander, there will be a considerable instantaneous change in the sail characteristic acceleration, as opposed to the gradual small change for the staggered deployment of the small ChipSat probes. It is shown that the Time-Delayed Feedback Control (TDFC) method is effective in controlling the orbit of the sail after this deployment. The sail converges to an orbit in the same region of phase space when deployment is made from both a lower and higher inclination orbit.

1. Introduction

Each mission to visit an asteroid seeks to answer some of the many unanswered questions about the origins of our solar system [1]. Additionally, each mission seeks to better understand the physical properties of these bodies such that we might better defend ourselves against the threat of an Earth impact [2]. As such, most of these missions have, and will, require some interaction with the surface of the asteroid.

There have already been several examples of the successful deployment of a lander from a spacecraft, as well as the landing of a spacecraft itself, to the surface of an asteroid. The first landing on an asteroid was performed in February 2001 by the NEAR-Shoemaker mission at asteroid Eros [3]. This landing was not a part of the set objectives but was improvised at the end of the mission. The Hayabusa mission to asteroid Itokawa brought about a sample return excursion to the surface in November 2005 [4]. A follow-up mission, Hayabusa2, made multiple successful surface interactions with the MINERVA II and MASCOT landers, as well as performing a sample return with the Hayabusa2 spacecraft itself. Most recently, the OSIRIS-REx mission successfully extracted a sample of asteroid Bennu in September 2020, which is now returning to Earth [5]. Most of these missions,

with notable exceptions such as the Dawn mission, have targeted a single body. However, advances in propulsion technologies make it possible to envision missions which can target multiple asteroids. This is made possible by the application of solar sail, and solar electric (SEP), technology [6–11]. Solar sails and SEP have also been proposed as a potential hybrid propulsion system when combined [12]. This combination allows the advantages of both systems to be exploited; the propellantless nature of the sail and the freedom to thrust in any direction with SEP. The combination of these systems also allowed for an increase in the delivered mass in a study for a mission to comet 45P [13]. This mission study also showed that the sail was predominantly useful for inclination changes, a notoriously propellant intensive manoeuvre which indicates the potential for this combined approach. In the near future, NASA will launch its NEA Scout, the first solar sail mission to flyby a Near-Earth Asteroid (NEA) [14].

A mission which seeks to interact with the surface of an asteroid must also deal adequately with the irregular gravity field generated by the uneven mass distribution of the small body. This uneven mass distribution has a considerable effect on the system dynamics within a

---

few body radii of the surface [15,16]. Outside of a few radii, it is sufficient to model the body as a point mass. There has been much work in the literature regarding the multi-body dynamics of the Sun–asteroid–spacecraft system. This model is referred to as Hill's problem [17], where the mass ratio of the smaller primary body to the larger primary body tends to zero. This body of work has shown the existence of families of periodic orbits [18–22], provided analysis of the motion of a solar sail [23,24], the limitations of a solar sail in the weak gravitational field of the asteroid [25] and shown the feasibility of controlling a solar sail around artificial equilibrium points [26], themselves displaced by the addition of the solar sail to the system dynamics.

When the spacecraft is close to the asteroid, within a few radii, it is necessary to take account of its irregular shape. However, it is possible to consider only the gravitational potential of the asteroid itself, given the relatively weak effect of the Sun. When the spacecraft is very close to the surface, an accurate shape model should be applied to take account of the true surface topology. A considerable body of work has been produced on the 2-body dynamics of an irregularly shaped body modelled using highly detailed polyhedron models [27–31]. However, these models require many thousands of calculations at each time step of a numerical integration. For initial work in which the effectiveness of a method is being tested, the computational expense involved is limiting. It has been shown in Ref. [16] that the "shape" of the gravitational potential field very quickly becomes ellipsoidal as the query point moves away from the body. As such, an ellipsoidal model is an appropriate choice for preliminary work. The Restricted Full 2-Body Problem (RF2BP) has been applied to such a problem where the C_{22} gravity coefficient, which provides the body ellipticity [32], is included to model the asteroid as an ellipsoid [33].

The problem of spacecraft motion on or near the surface of an asteroid has been widely treated in the literature [34–38] and will not form part of this work, but landing trajectories will be presented for completeness.

Farrés et al. [24] examined the problem of delivering a lander to the surface of one of Jupiter's Trojan asteroids from a solar sail spacecraft. Although this work addressed the problem of ensuring the lander remained on the asteroid surface, it did not study the problem at the point of lander separation and the control of the sail thereafter.

This paper will envisage two alternative mission scenarios: the first will be in the deployment of a series of small ChipSat-like probes [39] (hereby referred to simply as "ChipSat") from a stationary point, and the second will be the deployment of a single large MASCOT-type lander [40] from an orbit around an asteroid. Developed by DLR with close cooperation from CNES and JAXA, the MASCOT ("Mobile Asteroid Surface SCOuT") lander is a surface science platform that was successfully deployed as part of the JAXA Hayabusa2 mission to the surface of asteroid Ryugu [40].

A ChipSat is a centimetre-scale spacecraft contained on a printed circuit board (PCB). With the miniaturisation of technology, it is possible for the PCBs to contain inertial measurement units, attitude determination and control systems and wireless radio frequency communications [39]. In addition to hosting these systems, the high area-to-mass ratio of the ChipSat means that it can also produce thrust from SRP [41,42]. Their small size and mass make them very attractive to solar sail missions given the dependency on the sail performance to the area-to-mass ratio of the sailcraft. During deployment, the sail maintains a hover condition at a chosen (artificially sail-displaced) equilibrium point. The balance of forces required for the existence of an equilibrium point must consider the force contributed by the continuous acceleration of the sail. As each probe is released, the changing sail mass and hence acceleration means that this equilibrium point changes position. The control strategy is to maintain the sailcraft as close to the original hover point as possible. As each ChipSat is of a relatively small mass compared with the larger spacecraft, each release has a very small effect on the sail acceleration. As the resulting change in the system dynamics due to each probe release is expected to

Table 1
Dynamical regimes with the radius at which the regime applies in terms of asteroid mean radius (r_0) and associated dynamical models, shape models and reference frames.

	Outer regime	Inner regime
Regime operational radius	$>5r_0$	$\leq 5r_0$
Dynamical model	SSHR3BP	Two-body
Shape model	Point-mass	Ellipsoid/Polyhedron
Reference frame	Sun–asteroid synodic	Body-fixed

be small, this work will use and compare maintaining a fixed attitude with the use of a feedback controller, in this case a Linear Quadratic Regulator (LQR), for control after deployment [43,44].

For the deployment of the single large lander, the sail is in orbit closer to the asteroid surface. At the point of deployment, there is a single instantaneous large increase in the sail characteristic acceleration. The control strategy in this scenario is to maintain a bound orbit around the asteroid after this instantaneous increase in performance. As there is a considerable change to the dynamics, there is no reference trajectory for the LQR to follow. As such, a Time-Delay Feedback Control (TDFC) [33] is employed. This method does not require a reference trajectory as it takes the state of the spacecraft one period ago as the reference point at each time step.

This paper aims to show that a solar sail can be successfully controlled after the release of a probe or lander which results in an instantaneous, often considerable, change to the dynamics around the asteroid. Section 2 describes the dynamical models and frames of reference used throughout the paper. Section 3 discusses the control methods which are used. Section 4 describes the deployment of a series of small ChipSat probes from the sailcraft, and finally, Section 5 describes the deployment of the single large MASCOT-type lander from the sailcraft.

2. Dynamics

There are two dynamical models and three shape models used for the motion of the particle (this term generalises where the discussion may involve either the sailcraft or the lander/probe) around the asteroid used in this work, and each is applied depending on the distance at which the particle will operate with respect to the asteroid, and the corresponding dynamical regime in which it finds itself. There are two dynamical regimes in this work: the outer and inner regimes. Table 1 defines the radius at which each regime is applied as well as the corresponding dynamical models, shape models and reference frames, which will be discussed in the following sections.

When the particle is distant from the body ($>5r_0$, where r_0 is the mean asteroid radius), the asteroid shape has a negligible effect on the gravitational field [15], while the gravitational force from the Sun is not negligible; hence, a point-mass 3-body model (Solar Sail Hill's restricted 3-Body Problem, (SSHR3BP)), which includes the gravitational effect of the Sun as well as the effect from solar radiation pressure (SRP), is used. This region is referred to as the "Outer Regime". When the particle is within approximately five mean asteroid radii [16], a 2-body model will be used. This will be referred to as the "Inner Regime". In the inner regime, and when the trajectory of the particle will take it very close to the surface of the asteroid (i.e. for the analysis of impact on the surface), a high resolution polyhedron shape model will be applied. Otherwise, an ellipsoidal shape model is used. Subsequent sections here will describe each of the models used in this work, after an introduction to the different reference frames used.

2.1. Target asteroid

Although the work in this paper makes an attempt to generalise the results for application to any asteroid, it is necessary to define some
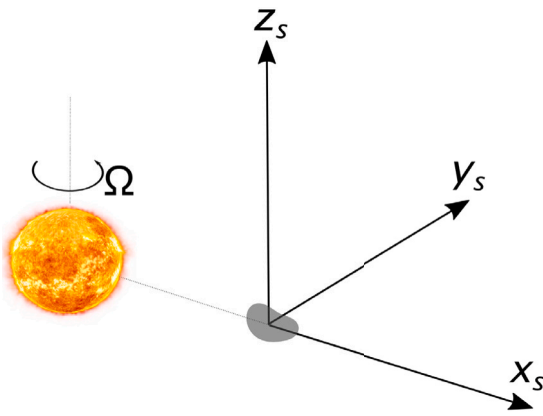
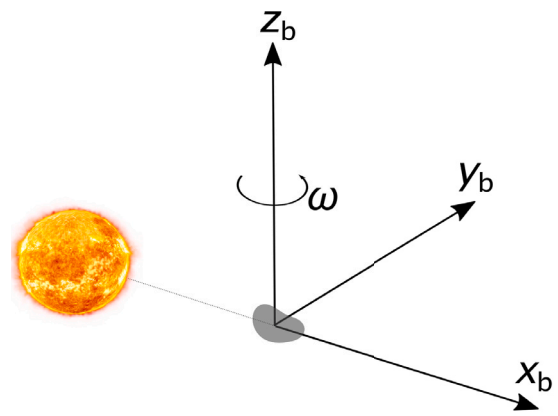**Fig. 1.** Synodic reference frame centred on the asteroid.

Fig. 2. Body-fixed reference frame.

physical parameters to enable simulations. Morrow and Scheeres [45] define upper limits for a size of sail which can maintain bound motion around an asteroid of a given size with the maximum characteristic acceleration (defined in Section 2.3), given as:

$$a_c^M = \frac{r_{au}^2}{16} \frac{\bar{\mu}}{r_0} \tag{1}$$

where r_{au} is the distance of the sun to the asteroid in AU and $\bar{\mu}$ is the asteroid gravitational parameter in dimensional units. This relationship also indicates that missions to asteroids further out in the solar system would allow the same sail to operate around smaller bodies, given the inverse square scaling for the magnitude of the sail acceleration (see Eq. (5)). The sail should also be suitable to perform the interplanetary transfer, although small sails have been shown capable of multi-asteroid rendezvous missions [11]. In order to avoid issues where the sail acceleration may be too large in the relatively weak gravitational field of a small asteroid, the decision was made to use a large body. In order to also provide analysis of trajectories very close to the asteroid surface, an asteroid which has been visited by a spacecraft and which contains a high resolution shape model was also sought. The asteroid Vesta met these conditions and the work throughout this paper will use the physical parameters (including the true mass) and shape model for this body. However, in order that the maximum acceleration available from the sail is maintained and remains constant, the asteroid orbit will be placed at 1 AU in a circular orbit. At this distance, the maximum available acceleration from the sail is the characteristic acceleration, a_c. An eccentric asteroid orbit would simply result in a varying magnitude of sail acceleration. The choice of Vesta is made purely for the physical parameters and available high resolution polyhedron shape model of that body and not out of interest in a mission specific to Vesta.

2.2. Frames of reference

This work utilises two main frames of reference: the synodic frame for the outer regime and the body-fixed frame for the inner regime.

The synodic reference frame, illustrated in Fig. 1, is centred on the asteroid centre of mass and rotates with the Sun–asteroid line, with the Sun's position fixed along the x-axis.

where Ω is the rotational velocity of the Sun–asteroid system. As the asteroid is at a considerable distance from the Sun, the Sun-sail line (which will be used for calculating the SRP) can be assumed equal to the Sun–asteroid line, and in the Synodic frame is given by:

$$\hat{\mathbf{S}} = [1, 0, 0] \tag{2}$$

The body-fixed frame is used in the inner regime where the gravitational effect from the Sun is ignored, but where the shape and the
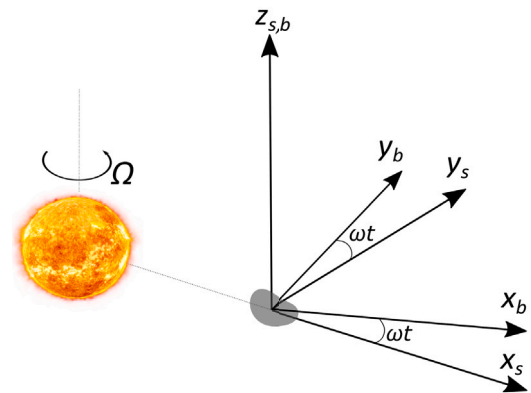

Fig. 3. Composite of synodic and body-fixed reference frames, centred on the asteroid, with rotation of the body-fixed frame at arbitrary time, t.

rotation of the asteroid play an important part in the gravitational field. The frame of reference is fixed on the asteroid centre of mass and rotates with it. As the frame is rotating, the position with the Sun appears to rotate around the asteroid and so the Sun-particle line is given by [23]:

$$\hat{\mathbf{S}} = [\cos(\bar{\omega}t), -\sin(\bar{\omega}t), 0]^T \tag{3}$$

where ω is the rotational velocity of the asteroid and the bar notation denotes dimensional units.

Where the shape model used is that of an ellipsoid, the x-axis is set along the largest dimension of the ellipsoid, the z-axis along the axis of rotation and the y axis completes the right-handed set. For a simple rotator of homogeneous density, the z-axis is also the shortest of the ellipsoid dimensions, with the y-axis being the next shortest which migrates into the equatorial plane. Where the high resolution polyhedron models are used, the axis directions are defined by the models which are obtained from observation data [46], with the z-axis always along the axis of rotation. At $t = 0$, the body-fixed frame is aligned with the synodic frame, with the Sun in the negative x_b direction. The relative orientations of the synodic and body-fixed frames are demonstrated in Fig. 3.

Additionally, where appropriate, trajectories are presented in an asteroid-centred inertial frame. This frame is used solely for the presentation data, as well as calculation of classical orbital elements, and is not used in any of the various simulations.

2.3. Solar sail model

A solar sail is a large thin membrane which provides thrust by reflecting photons radiated by the Sun. This reflection results in a
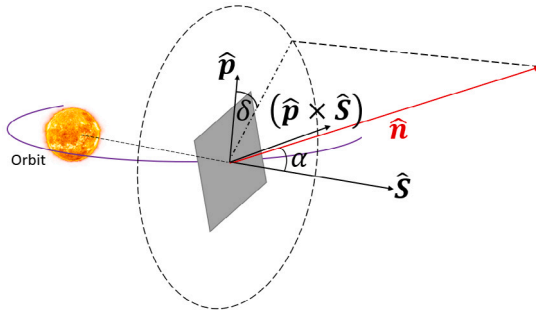
Fig. 4. Solar sail attitude definition.

momentum transfer from the photon to the sail. The performance metric of the sail used in this work is the characteristic acceleration, a_c, defined as the acceleration experienced by the sail at 1 AU when the unit normal vector from the surface of the sail is parallel to the Sun-sail line. This performance metric depends on the area-to-mass ratio of the sailcraft. As a comparison to the traditional metric in mission analysis, ΔV, the sail can be considered capable of providing $\Delta V = \|\mathbf{a}\|t$, where $\|\mathbf{a}\|$ is the magnitude of the acceleration provided by the sail and t is the thrusting time. At 1 AU, and with the sail unit normal vector parallel with the Sun-sail line, the sail provides its maximum $\Delta V = a_c t$.

The sail provides a continuous thrust from SRP. although there have been studies of furlable sails [47], the technological challenges involved in this are considerable. As such, the only method of "turning off" a sail, is for the attitude to be side-on to the Sun ($\alpha = 90°$). To achieve this, an on-board ADCS system capable of not only placing the sail into this attitude, but also recovering the sail from it, would be required.

Fig. 4 shows the angles which define the sail attitude: the cone angle, α, and the clock angle, δ. The unit vector $\hat{\mathbf{S}}$ gives the radial direction from the Sun to the sail and $\hat{\mathbf{p}}$ is the unit vector normal to the orbit plane [48]. The sail itself is centred on the $[\hat{\mathbf{S}}, \hat{\mathbf{p}} \times \hat{\mathbf{S}}, \hat{\mathbf{p}}]$ frame. The angle between the Sun-sail line, $\hat{\mathbf{S}}$, and the sail normal, $\hat{\mathbf{n}}$, is referred to as the cone angle. Projecting the unit vector $\hat{\mathbf{n}}$ back to the $[\hat{\mathbf{p}}, \hat{\mathbf{p}} \times \hat{\mathbf{S}}]$ plane, the angle of rotation around the $\hat{\mathbf{S}}$ axis to that point, starting from the $\hat{\mathbf{p}}$ axis, is referred to as the clock angle. With $\delta \in [0, 2\pi]$ and $\alpha \in [0, \pi/2]$, the sail attitude can be fully defined by these two angles. The control can also be defined in terms of the radial, transversal and normal components:

$$\hat{\mathbf{n}} = \cos(\alpha)\hat{\mathbf{S}} + \sin(\alpha)\sin(\delta)\hat{\mathbf{p}} \times \hat{\mathbf{S}} + \sin(\alpha)\cos(\delta)\hat{\mathbf{p}} \tag{4}$$

As the sail in this work is considered to be perfectly reflecting and flat, the sail normal unit vector $\hat{\mathbf{n}}$ is coincident with the sail thrust vector. Imperfections in sail reflectivity can be accounted for in a reduction in the magnitude of the sail acceleration. Billowing of the sail material has also been studied for more detailed mission analysis in Ref. [49] where the thrust vector will not align with the sail unit normal vector, and so where the trajectory will be affected. However, for this higher level initial study, the ideal model is considered sufficient. Therefore, the sail control can be defined either in terms of the cone and clock angles, or in terms of $\hat{\mathbf{n}}$, where the sail acceleration is given by [23]:

$$\mathbf{a} = a_c \left(\hat{\mathbf{S}} \cdot \hat{\mathbf{n}}\right)^2 \hat{\mathbf{n}} \tag{5}$$

As the orbit of the asteroid is at 1 AU, the characteristic acceleration does not require to be scaled in this expression. At distances greater or smaller than 1 AU, the inverse square scaling of the SRP must be considered. Eclipses are simulated as discussed in Ref. [50], and outlined in Fig. 5.

The angle of umbra is given by:

$$\sin(\theta_{umb}) = \frac{r_s - r_p}{R_p} \tag{6}$$

where r_s is the radius of the Sun, r_p is the radius of the planet or body and R_p is the distance between the Sun and the planet/body. The vertical length of the umbra region is then calculated by:

$$umb_{vert} = \tan(\theta_{umb})(y - sat_{horiz}) \tag{7}$$

where $y = \frac{r_p}{\sin(\theta_{umb})}$ and sat_{horiz} is the component of the satellite position in the ecliptic plane. When the spacecraft is on the half of its orbit in which the umbra region exists, and when $sat_{vert} \leq umb_{vert}$, the spacecraft is deemed to be in umbra. Where the sail is in umbra, the sail acceleration is set to zero. As such, there exist ballistic arcs along each orbit.

2.4. Outer regime

In the case of the Sun–asteroid–spacecraft system, the vanishingly small mass ratio enables use of the Hill's Restricted 3-Body Problem (HR3BP) [17]. In the HR3BP dynamical model, the synodic reference frame described in Section 2.2 is used. The HR3BP is normalised using the Hill radius, which gives length unit:

$$L = \left(\frac{\bar{\mu}}{3\bar{\Omega}^2}\right)^{\frac{1}{3}} \tag{8}$$

where $\bar{\mu}$ is the asteroid gravitational parameter, $\bar{\Omega}$ is the rotational velocity of the Sun–asteroid system and the bar notation denotes dimensional units. Time units are normalised by $T = \bar{\Omega}^{-1}$. The non-dimensional equations of motion for the Solar Sail HR3BP (SSHR3BP) are therefore given by [45]:

$$\ddot{x}_s = 2\dot{y}_s - \frac{\mu}{r_s^3}x_s + 3x_s + a_{x_s}$$
$$\ddot{y}_s = -2\dot{x}_s - \frac{\mu}{r_s^3}y_s + a_{y_s} \tag{9}$$
$$\ddot{z}_s = -\frac{\mu}{r_s^3}z_s - z_s + a_{z_s}$$

where $r_s = \sqrt{x_s^2 + y_s^2 + z_s^2}$ and the sail acceleration ($\mathbf{a}_s = [a_{x_s}, a_{y_s}, a_{z_s}]$) is given by Eq. (5).

The continuous acceleration provided by the momentum transfer from photon to sail has a considerable effect on the dynamics of the 3-body system, not least of which is a positional change in the system equilibrium points. This work will leverage such artificially displaced equilibrium points (AEPs) of the restricted 3-body problem. These AEPs provide convenient deployment locations for probes sent towards the surface of the asteroid. The equilibrium points of the system are obtained from:

$$0 = -\frac{\mu}{r_s^3}x_s + 3x_s + a_{x_s}$$
$$0 = -\frac{\mu}{r_s^3}y_s + a_{y_s} \tag{10}$$
$$0 = -\frac{\mu}{r_s^3}z_s - z_s + a_{z_s}$$

This can also be written in vector form as:

$$\nabla U_s = -\mathbf{a}_s \tag{11}$$

where U_s is the effective gravitational potential in the synodic frame of the HR3BP. The sail orientation can then be obtained from [23,51]:

$$\hat{\mathbf{n}}_s = -\frac{\nabla U_s}{|\nabla U_s|} \tag{12}$$

With this, it is possible to calculate the required sail characteristic acceleration to maintain an AEP for a particular sail attitude from:

$$a_c = -\frac{\nabla U_s \cdot \hat{\mathbf{n}}_s}{(\hat{\mathbf{S}}_s \cdot \hat{\mathbf{n}}_s)^2} \tag{13}$$

Now, the contours of a_c for asteroid Vesta can be established [23,45]. These contours contain the AEPs for each value of a_c at different sail
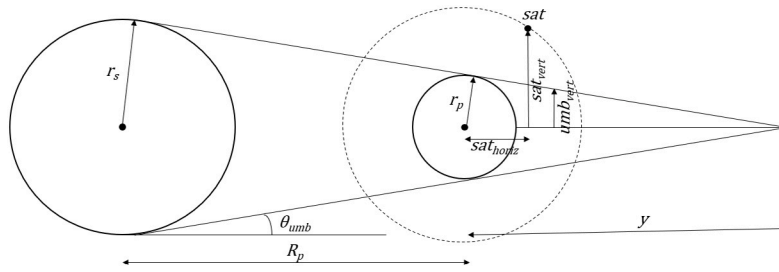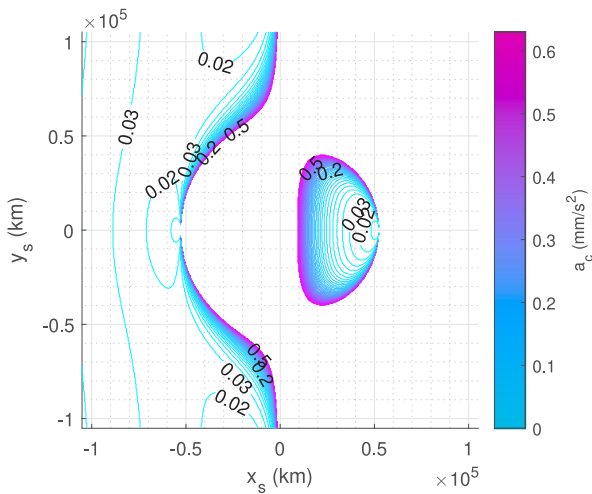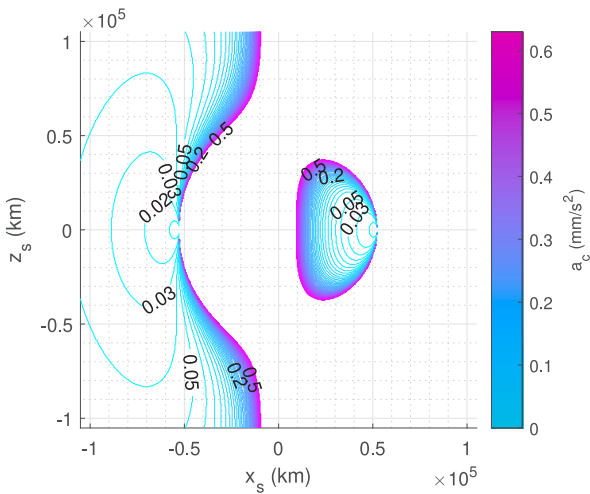
Fig. 5. Eclipse model, as given in Ref. [50].

(a) x-y plane

(b) x-z plane

Fig. 6. Contours of AEPs for varying characteristic acceleration.

orientations, and are shown in Fig. 6. It should be noted that those AEPs which exist in the eclipse region are still shown here.

The natural equilibrium points, Lagrangian points L_1 and L_2, are indicated in Fig. 6. It can be seen that the inability of the sail to produce thrust in the direction of the Sun limits the range of AEPs to lie on the Sun-side of the natural equilibrium points. The L_2 AEPs are all contained in the enclosed region shown between the natural L_2 point and the asteroid, and the L_1 AEPs are all contained on the solar side of the asteroid.
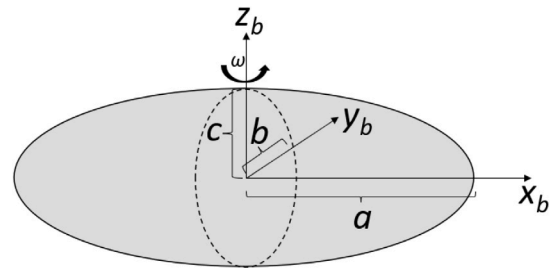

Fig. 7. Ellipsoid dimensions in the body-fixed frame.

2.5. Inner regime

For operations in the inner regime, where the particle (either sail-craft or lander/probe) is not approaching the asteroid surface, an ellipsoidal model will be implemented in the Restricted Full 2-Body Problem (RF2BP) [52]. In this problem, the mass ratio of the small body to the large tends to zero, the case for a massless particle orbiting the large primary. The potential function for the RF2BP is given by:

$$V_b = -\frac{1}{\sqrt{x_b^2 + y_b^2 + z_b^2}} - \frac{1}{2}\left(x_b^2 + y_b^2 + z_b^2\right) + U_b \tag{14}$$

where U_b is the potential due to the non-spherical shape of the asteroid in the body-fixed frame. The non-dimensional equations of motion for the RF2BP in the body-fixed frame are given by:

$$
\begin{aligned}
\ddot{x}_b - 2\dot{y}_b &= -\frac{\partial V_b}{\partial x_b} \\
\ddot{y}_b - 2\dot{x}_b &= -\frac{\partial V_b}{\partial y_b} \\
\ddot{z}_b &= -\frac{\partial V_b}{\partial z_b}
\end{aligned}
\tag{15}
$$

To consider a simple ellipsoidal potential, the sectoral harmonic [50] C_{22} gravity coefficient can be used [33,52]. It is possible to define the C_{22} gravity coefficient from the dimensions of the ellipsoidal body. The ellipsoid dimensions are shown in Fig. 7. Using these dimensions, the gravity coefficient is given by [53]:

$$\bar{C}_{22} = \frac{1}{20\bar{r}_0^2}\left(\bar{a}^2 - \bar{b}^2\right) \tag{16}$$

where r_0 is the ellipsoid mean radius. The normalised gravity coefficient is then given by:

$$C_{22} = \left(\frac{\bar{\mu}}{\bar{\omega}^2}\right)^{-\frac{2}{3}} \bar{r}_0^2 \bar{C}_{22} \tag{17}$$

The non-dimensional ellipsoidal potential is then given by [33,52]:

$$U_{b_e} = -\frac{3\, C_{22}\left(x_b^2 - y_b^2\right)}{\left(x_b^2 + y_b^2\right)^{5/2}} \tag{18}$$

which can be included in the potential function:

$$V_b = -\frac{1}{\sqrt{x_b^2 + y_b^2 + z_b^2}} - \frac{1}{2}\left(x_b^2 + y_b^2 + z_b^2\right) + U_{b_e} \tag{19}$$

A system of normalisation [32] then sets the reference length as the orbital radius of a 1:1 synchronous orbit around a spherical body of the same mass as the asteroid in question:

$$L = \left(\frac{\bar{\mu}}{\bar{\omega}^2}\right)^{\frac{1}{3}} \tag{20}$$

Time is then normalised by $T = \bar{\omega}^{-1}$. It is clear that, for very slow rotators, the unit of length may have a very large value. In order for the length units of this normalisation to reach the radius of the Hill sphere (Eq. (8)), the rotational velocity would need to take a value of $\bar{\omega} = \sqrt{3}\bar{\Omega}$. In fact, the slowest known rotator, asteroid 288 Glauke, has a rotational velocity of $\bar{\omega} = 1.4917 \times 10^{-6}$ rad/s and an orbital angular velocity of $\bar{\Omega} = 4.3422 \times 10^{-8}$ rad/s. As such, this gives a rotation to orbit angular velocity ratio of $\frac{\bar{\omega}}{\bar{\Omega}} = 34.3536$, much larger than the value of $\sqrt{3}$ at which the length unit would equal the Hill radius. If the situation were to arise, it would most likely do so for a very slow rotating asteroid in the inner solar system where the Hill radius is reduced.

Although the asteroid considered here is a simple rotator with constant rotational velocity around the z-axis only, there are also complex rotators which rotate around all axes. It has been shown that these complex rotations can be averaged using a set of secular equations of motion which, over short time-spans, have good agreement with the full dynamics of the complex rotation [54].

When considering the landing trajectories of the probes/lander, the shape model obtained in Ref. [55] is applied. The gravitational potential for a polyhedron in the body-fixed frame is given by [53]:

$$U_{b_p} = \frac{1}{2}G\rho\left(\sum_{e \in \text{edges}}\left(\mathbf{r}_e \cdot \mathbf{E}_e \cdot \mathbf{r}_e\right)L_e - \sum_{f \in \text{faces}}\left(\mathbf{r}_f \cdot \mathbf{F}_f \cdot \mathbf{r}_f\right)\gamma_f\right) \tag{21}$$

where ρ is the body mean density, $\mathbf{E}_e$ is a dyad defined in terms of the face and edge normal vectors associated with each edge, L_e is a logarithmic term expressing the potential of a 1-D straight wire, $\mathbf{F}_f$ is a dyad defined for each face as the outer product of the face unit normal with itself and γ_f is the signed solid angle subtended by a face when viewed from the field point [56].

The effective potential takes into account both the gravitational potential as well as the rotation of the asteroid, and is given by [57]:

$$V_b = \frac{1}{2}(\boldsymbol{\omega} \times \mathbf{r}) \cdot (\boldsymbol{\omega} \times \mathbf{r}) + U_{b_p} \tag{22}$$

where $\boldsymbol{\omega}$ is the vector of the rotational velocity of the asteroid and rotation is around the z-axis of the body fixed frame only. The Cartesian position of the particle relative to the body-fixed reference frame is given by $\mathbf{r}$. This shape model can then be included in the dynamical model for the spacecraft motion using Eq. (15)

3. Control methods

To affect appropriate control of the sail during the two stated mission scenarios, three methods of control will be used: Linear Quadratic Regulator (LQR), Genetic algorithm (GA) and Time-Delay Feedback control (TDFC).

For the multiple-ChipSat deployment, the LQR is compared with the performance of a fixed attitude sail during deployments, providing insight into the efficiency and efficacy of a simple fixed attitude and an optimal feedback controller.

In the MASCOT-type lander scenario, the GA is used to establish the necessary control law for a periodic orbit close to the asteroid. This is taken as the pre-deployment orbit. After the deployment of the lander, the pre-deployment orbit no longer exists in the new post-deployment dynamics. As such, there is no reference orbit along which to apply the LQR control, as desired. For this reason, the TDFC is applied as it uses the same optimal control framework as the LQR, but uses the state one period in the past as the reference. This allows the TDFC to find a bound orbit around the asteroid after lander deployment without depending on a reference trajectory to do so, ideal for the case where the change in dynamics would render any previous trajectory obsolete in the new dynamics.

3.1. Linear Quadratic Regulator (LQR)

The LQR is applied to the first mission scenario to maintain a hover position during ChipSat deployment. As the LQR requires that the equations of motion, outlined for the different dynamical models in Section 2, are re-written as a first-order differential system, $\dot{\mathbf{s}} = \mathbf{f}(t, \mathbf{s})$. The linear dynamics are given by [44]:

$$\delta\dot{\mathbf{s}}(t) = \mathbf{A}(t)\delta\mathbf{s}(t) + \mathbf{B}\mathbf{u}(t) \tag{23}$$

where $\delta\mathbf{s}(t)$ is the error between the current state and the reference state at time, t, and:

$$\mathbf{A}(t) = \begin{bmatrix} \mathbf{0} & \mathbf{I} \\ \mathbf{V}'' & -\boldsymbol{\Omega} \end{bmatrix} \tag{24}$$

and $\mathbf{0}$ is a 3×3 matrix of zeros, $\mathbf{I}$ is a 3×3 identity matrix, and:

$$\boldsymbol{\Omega} = \begin{bmatrix} 0 & -2 & 0 \\ 2 & 0 & 0 \\ 0 & 0 & 0 \end{bmatrix} \quad \mathbf{V}'' = \begin{bmatrix} \frac{\partial^2 V}{\partial x^2} & \frac{\partial^2 V}{\partial xy} & \frac{\partial^2 V}{\partial xz} \\ \frac{\partial^2 V}{\partial yx} & \frac{\partial^2 V}{\partial y^2} & \frac{\partial^2 V}{\partial yz} \\ \frac{\partial^2 V}{\partial zx} & \frac{\partial^2 V}{\partial zy} & \frac{\partial^2 V}{\partial z^2} \end{bmatrix} \tag{25}$$

$$\mathbf{B} = \begin{bmatrix} 0 & 0 & 0 & 1 & 0 & 0 \\ 0 & 0 & 0 & 0 & 1 & 0 \\ 0 & 0 & 0 & 0 & 0 & 1 \end{bmatrix}^T \tag{26}$$

This system approximates the real system at a given time and close to the reference trajectory. In order to establish an optimal feedback control law, the following objective function is used:

$$J(\mathbf{u}, t) = \int_0^\infty \left(\delta\mathbf{s}(t)^T \mathbf{Q}\delta\mathbf{s}(t) + \mathbf{u}(t)^T \mathbf{R}\mathbf{u}(t)\right) dt \tag{27}$$

where $\mathbf{Q}$ and $\mathbf{R}$ are weighting matrices which account for the cost of each state and control. The required control is then obtained from Ref. [44]:

$$\mathbf{u}(t) = -\mathbf{K}\delta\mathbf{s} \tag{28}$$

Minimisation of Eq. (27) leads to the algebraic Riccati equation (shown in Eq. (32)) [58] which is solved to give the gain matrix $\mathbf{K}$.

3.2. Genetic algorithm

The purpose of using the GA in this work is to provide a means of finding an optimal control law where an initial guess close enough to the optimal solution is difficult to obtain. In this work, the GA is used to find a control law which facilitates a periodic orbit close to the asteroid for the deployment for a large MASCOT-type lander.

The GA provides a method for both constrained and unconstrained optimisation based on the principles of evolution. Having defined "individuals" that encode the solution vector, the algorithm combines pairs of "parents" to produce the next generation of "children". Over successive generations, the "population" will converge to the optimal solution [16].

The benefit of this algorithm, for the purposes of this work, is that it requires no initial guess from the user. The algorithm can be initialised with an initial population randomly spread in the search space. However, it is important to note that the algorithm is stochastic, and the convergence to the global optimum is not guaranteed; in fact, a solution provided from one initial population can be different from

the optimal solution for another initial population. As such, it is often necessary to run multiple instances, or "seeds", in order to obtain a true optimal solution.

In the search for a periodic pre-deployment orbit for the MASCOT-type lander deployment, 10 seeds are initiated with that which produces the minimum objective value selected as the optimal solution. The objective function is given by:

$$J = \|\mathbf{s}_f - \mathbf{s}_0\| \tag{29}$$

with constraints placed on the sail attitude such that the sail normal points away from the Sun. The solution vector is encoded with the sail unit normal vector, orbital period and the initial Cartesian state for the orbit. The continuous time problem is discretised by twenty nodes with spline interpolation employed in the control. The objective is to obtain a periodic orbit. As such, the initial state is free within bounds to facilitate this search in the phase space.

3.3. Time-Delay Feedback Control (TDFC)

Time-delayed Feedback Control (TDFC) is a method for stabilising unstable periodic orbits [33,59]. This method of control lends itself well to the second mission scenario where a periodic orbit will be perturbed by the instantaneous increase in a_c. The required control is obtained by.

$$\mathbf{u}(t) = -\mathbf{K}\left(\mathbf{s}(t) - \mathbf{s}(t - \tau)\right) \tag{30}$$

where τ is the period of the orbit and $\mathbf{K}$ is the gain matrix. A such, the only orbital parameter which is required to be defined *a priori* is the orbital period.

In order for the TDFC to drive the trajectory onto a periodic orbit, a suitable matrix $\mathbf{K}$ is required. This can be calculated in the same process as that outlined in Section 3.1 and detailed here:

$$\mathbf{K} = \mathbf{R}^{-1}\mathbf{B}^T\mathbf{P}(t) \tag{31}$$

where $\mathbf{R}$ is a real symmetric positive definite matrix, $\mathbf{B}$ is a constant $n \times m$ matrix where m is the number of controls and n is the dimension of $\mathbf{s}(t)$, and $\mathbf{P}(t)$ is the solution of [58]:

$$\dot{\mathbf{P}}(t) = \mathbf{P}(t)\mathbf{B}\mathbf{R}^{-1}\mathbf{B}^T\mathbf{P}(t) - \mathbf{A}(t)^T\mathbf{P}(t) - \mathbf{P}(t)\mathbf{A}(t) - \mathbf{Q} \tag{32}$$

$\mathbf{Q}$ is a real symmetric positive definite matrix. Eq. (32) must then be integrated simultaneously with the equations of motion with $\dot{\mathbf{P}}(0) = 0$, $\mathbf{Q} = \mathbf{I}_{n \times n}$ and $\mathbf{R} = \beta\mathbf{I}_{m \times n}$. The free parameter, β, is the weighting parameter which allows the optimal preference to be shifted between minimising the effort required to force the periodic orbit, and the best periodic solution.

4. ChipSat deployment

The first mission scenario is that of deploying a series of small ChipSat probes. The deployment of the ChipSats will be performed at a distance from the asteroid where each ChipSat probe is sent towards the asteroid surface. As the sailcraft remains in the outer regime, the point mass SSHR3BP model is used for analysis of the sail control strategy, where impact trajectories will be analysed in the inner regime using the high resolution polyhedron shape model for accurate dynamics down to the surface.

4.1. Effect of ChipSat deployment on system dynamics

Assuming a 12U CubeSat bus, with 3U dedicated to carrying a payload of ChipSats, it is estimated that 20 ChipSats can be accommodated. The bus and sail parameters are detailed in Table 2 with those for the bus taken from Ref. [60].

The value of characteristic acceleration shown in Table 2 was chosen so as to link with other works related to the interplanetary

Table 2
Sailcraft physical parameters.

Parameter	Value
Bus mass	24.0 kg
ChipSat mass	10.0 g
No. of ChipSats	20
Bus and Payload mass	24.2 kg
a_c	0.2 mm/s²
Sail area	679.8 m²
Sail areal density	10 g/m²
Sail mass	6.8 kg
Total sailcraft mass	31.0 kg
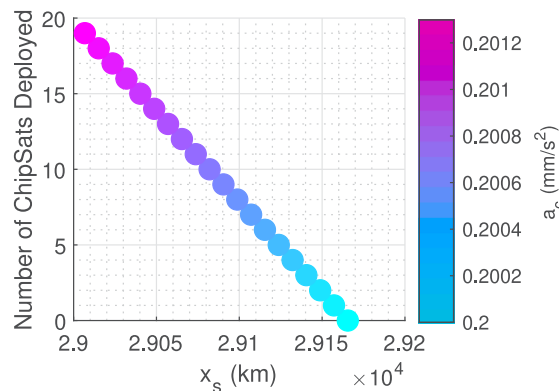
Fig. 8. Changing sail performance and AEP position with deployment of ChipSats.

phase of a multi-asteroid rendezvous mission [6,8]. By maintaining the same value as shown by those authors, the current work can be proposed as a direct connection to that phase of the mission. The same value was also proposed in Ref. [61] for a multi-asteroid rendezvous. Indeed, many authors have proposed solar sail missions with higher performance sails [62–65]. The value of sail areal density is considered possible for sails in the near-future [66].

As the acceleration of the sail is dependent on the sailcraft area-to-mass ratio, each time a ChipSat is released, there is a corresponding increase in sail acceleration. Fig. 8 shows the changing characteristic acceleration as the ChipSats are released. Due to the small mass of each ChipSat released, the change in a_c is also small. In fact, such changes could also be caused by degradation of the sail material over time. As such, it could be possible for the control methods used here to also be used to account for these effects. With this change in sail acceleration, there is a corresponding change to the dynamics and a unique set of AEPs is available for each value of the characteristic acceleration, which is also shown in Fig. 8.

4.2. ChipSat descent trajectory analysis

This section presents the trajectories and landing conditions of those ChipSats which reach the surface of the asteroid. To do this, five deployment locations are chosen and are listed in Table 3. The locations are dictated by the attitude of the sail and symmetrical locations in the y and z directions are chosen. These locations can be maintained by rotating the sail by $\alpha = \pm 45°$ with $\delta = 90°$ for locations 2 and 3, and $\delta = [0, 180]°$ with $\alpha = 0°$ for locations 4 and 5. This range of selected deployment locations offer the sailcraft different viewing angles of the surface of the asteroid.

In fact, it was found that location 1 exists in the eclipse region. As such, this would not be a feasible deployment location given that the sail would be incapable of providing thrust. However, the data for this deployment point are maintained here. As the trajectories will take the probes to the asteroid surface, the polyhedron shape model is applied when the ChipSats enter the inner regime.

(a) Outer regime (Synodic frame)
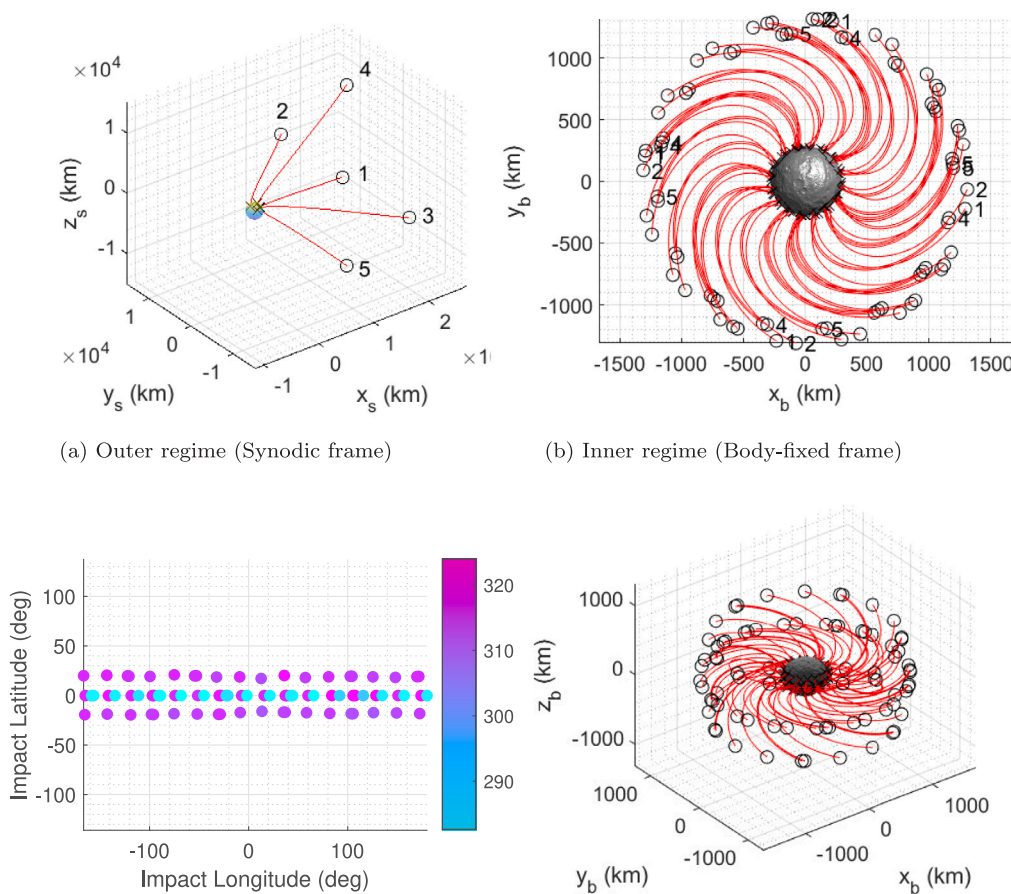

(b) Inner regime (Body-fixed frame)

Fig. 9. ChipSat trajectories in the outer and inner regions.

Table 3
Hovering locations in the synodic frame and sail attitude for ChipSat deployment.

Location	x_s (km)	y_s (km)	z_s (km)	$\hat{n}_{s_x}$	$\hat{n}_{s_y}$	$\hat{n}_{s_z}$
1	15,879	0	0	1	0	0
2	16,387	15,135	0	0.7071	0.7071	0
3	16,387	−15,135	0	0.7071	−0.7071	0
4	16,678	0	14,996	0.7071	0	0.7071
5	16,678	0	−14,996	0.7071	0	−0.7071

Fig. 9a shows the descent trajectories of the ChipSats in the outer regime, where the trajectories appear as direct descents towards the surface. At the point which the ChipSat crosses into the inner regime, the trajectories are affected by the rotation and the shape of the asteroid.

It is found that deployment locations 1, 2, 4 and 5 successfully deploy all 20 of the ChipSats to the surface of the asteroid. However, location 3, as it trails the asteroid direction of rotation, does not successfully deploy any of its compliment of ChipSats to the surface. As such, those trajectories shown in Fig. 9b and c are only those which successfully reach the surface. Fig. 9b also contains the deployment location number for a selection of the trajectories. Those which do not impact the surface are shown in Fig. 10. These trajectories approach close to the surface but then begin a spiralling escape trajectory, demonstrated by the crosses which denote the trajectory final points.

Although not considered in this work, the ChipSats themselves, if of a sufficiently high area-to-mass ratio or operating in a very weak gravity field, could experience significant effects from SRP.

The velocity upon impact is also provided here. The main work of the ChipSats is envisaged to be done during their descent, but their

probability of survival on the surface will depend on the impact conditions, which is dependent on the size of the asteroid. Fig. 9c gives the impact locations and velocities, and shows that in-plane deployments provide both some of the highest and lowest velocity impacts. On closer inspection of the results, the deployments from the AEP which lies on the x-axis give the highest velocity impacts. The lowest velocity impacts come from the in-plane deployment at the position which leads the asteroid rotation. These trajectories benefit from a lower velocity relative to the asteroid at the point of entry to the inner regime than those which lie along the x-axis of the outer regime. Given the high velocities, it is not expected that the ChipSats will survive impact. Assuming a ChipSat could survive similar impact velocities of a cellular telephone on Earth (≤ 4.427 m/s [67]), then an asteroid with a ratio of $\frac{\mu}{r_0} \leq 9.7992$ m²/s² would be the largest body from which deployment could be made from the locations described here and the ChipSats survive impact.

4.3. Sail control during deployment

The sail control law will now be established for the deployment of 20 ChipSats with a separation of one hour between each, from the five different deployment locations of Table 3. Although this separation is chosen arbitrarily here, it may be that mission designers choose to separate the probes for a specific mission objective, or perhaps even to be in resonance with the sail membrane. Given the relatively small mass of each ChipSat to the overall mass of the sailcraft, the reaction of each ChipSat release on the sailcraft is not considered here.

4.3.1. Fixed attitude

In the first instance, the sail attitude remains fixed in the synodic frame as set out in Table 3. The drift of the sail from the initial hover
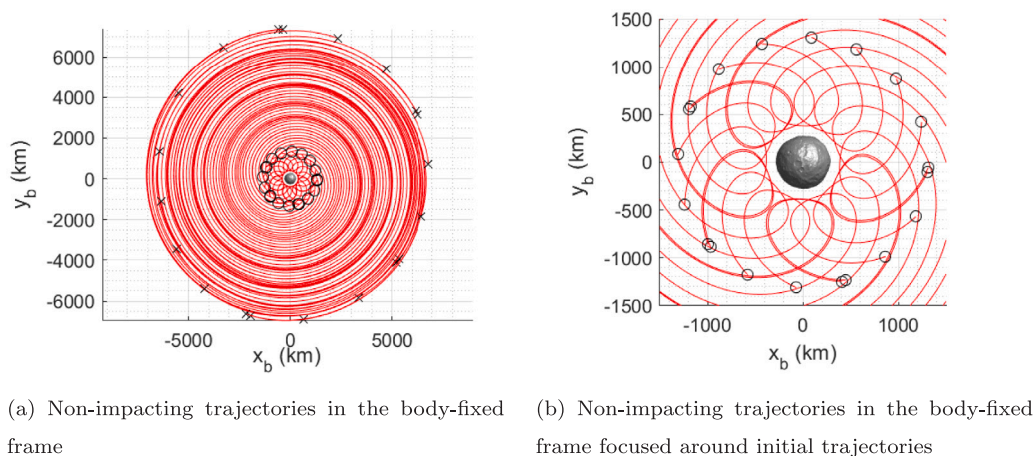
(a) Non-impacting trajectories in the body-fixed frame

(b) Non-impacting trajectories in the body-fixed frame focused around initial trajectories

Fig. 10. ChipSat trajectories which do not impact the surface of the asteroid.
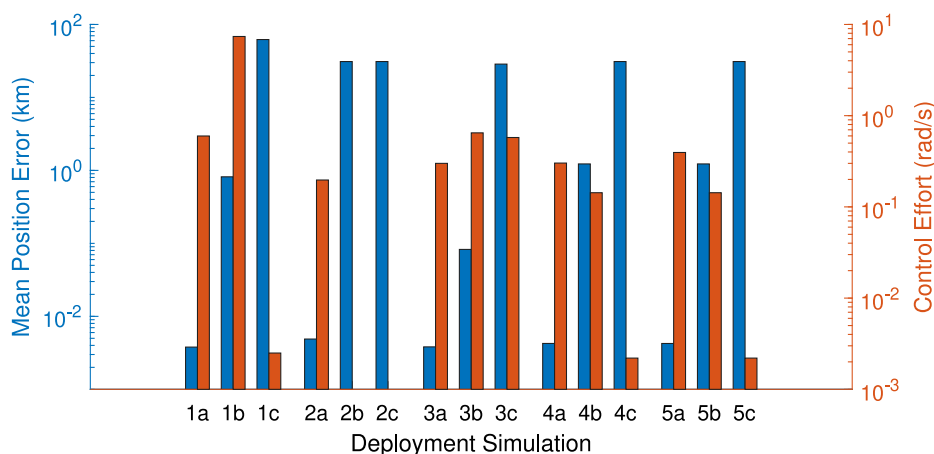

Fig. 11. Position error vs. control effort for each deployment simulation using LQR.

point is presented in Table 4. With the increasing sail acceleration after each ChipSat is released, the fixed attitude sail moves slowly away from the initial deployment point. Although there is some movement of the sail away from the initial point, the distance moved over the full deployment of all ChipSats is still relatively small.

4.3.2. Linear quadratic regulator

Following the fixed attitude simulation, the use of LQR control to maintain the initial hover location is analysed. For each deployment point of Table 3, there will be three associated simulations (*a*, *b* and *c*), each related to a different weighting on the **Q** and **R** matrices. In all simulations, $\mathbf{Q} = \mathbf{I}_{6\times6}$ and $\mathbf{R} = \beta \mathbf{I}_{3\times3}$. Here, $\beta_a = 1 \times 10^{-6}$, $\beta_b = 1$ and $\beta_c = 1\times10^6$ for simulations *a*, *b* and *c* respectively. The three simulations give examples where the states are given greater weighting than the control effort in the LQR controller (simulation *a*), where the states and effort are given equal weighting (simulation *b*) and where the control effort is given greater weighting (simulation *c*). The mean position error is calculated by taking the mean of the scalar error between the final position at the end of each 1-h deployment phase and the reference point. The control effort is a scalar value obtained by performing a trapezoidal integration of the angular accelerations of the control law resulting from each simulation. The integral gives the total changes in slew rate of the sail during deployment, and is measured in radians per second. The results in terms of the mean position error and control effort are given in Fig. 11.

It is clear from Fig. 11 that the control effort required does not necessarily reduce for simulation *b* when compared to simulation *a*.

A reduction in control effort requires that the weighting is far more biased towards the **R** matrix, such as in simulation *c*. Where this is the case, it is possible to achieve very low values of control effort, as in simulations 2*b* and 2*c*.

Fig. 11 shows that it is possible to achieve a very small positional error with respect to the initial hover point, at a cost of higher effort required by the sail control system. By reducing the sail control effort, there is an increase in the positional error. For very small values of control effort, there can be considerable positional error values. These errors are far greater than those where the sail remains with a fixed attitude during deployment, as seen in Table 4. As an example of the LQR performance, the results from simulation *a* are used for comparison with the fixed attitude in Table 4, which give the most weight to maintaining the hover position for a higher control effort. The control laws from this simulation are given in Fig. 12. We note that viewing angle changes, due to the displacement from the original hover location, are small enough that they would not be a problem for scientific remote observation.

4.3.3. Comparison of methods

The results of Table 4 show that the LQR control is the most capable of maintaining the sail close to the original hover location.

However, the considerable extra effort required by the sail to follow the LQR control does not bring about such an improvement in performance to warrant its inclusion on a real mission. As such, for a real scenario, the recommendation would be to use a fixed sail attitude during ChipSat release. Where the sail acceleration becomes
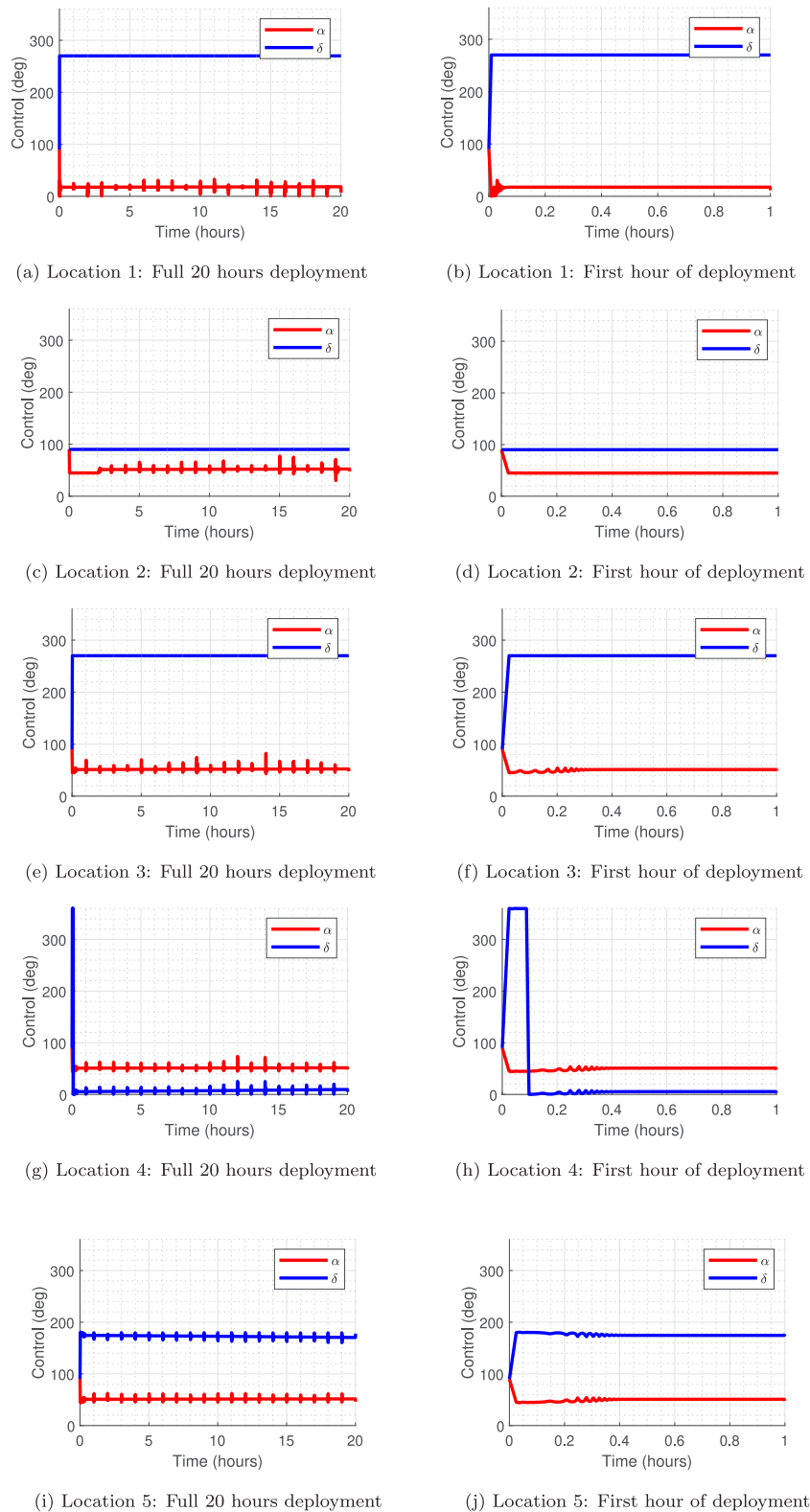
Fig. 12. LQR control during hover for ChipSat deployment from all locations of Table 3.

more powerful relative to the asteroid gravitational acceleration, the fixed attitude would result in greater divergence from the desired deployment location. This may also be the case where the ChipSats may have a considerably larger mass than those of 10 g which are considered here. In these situations, it may be worth revisiting a control provided by the LQR.

5. MASCOT-type lander deployment

A MASCOT-type lander carries a much greater mass than the Chip-Sats deployed in Section 4, and its release will result in a far more considerable change in a_c and consequently in the dynamics of the inner regime. As this is a single deployment, the change in dynamics
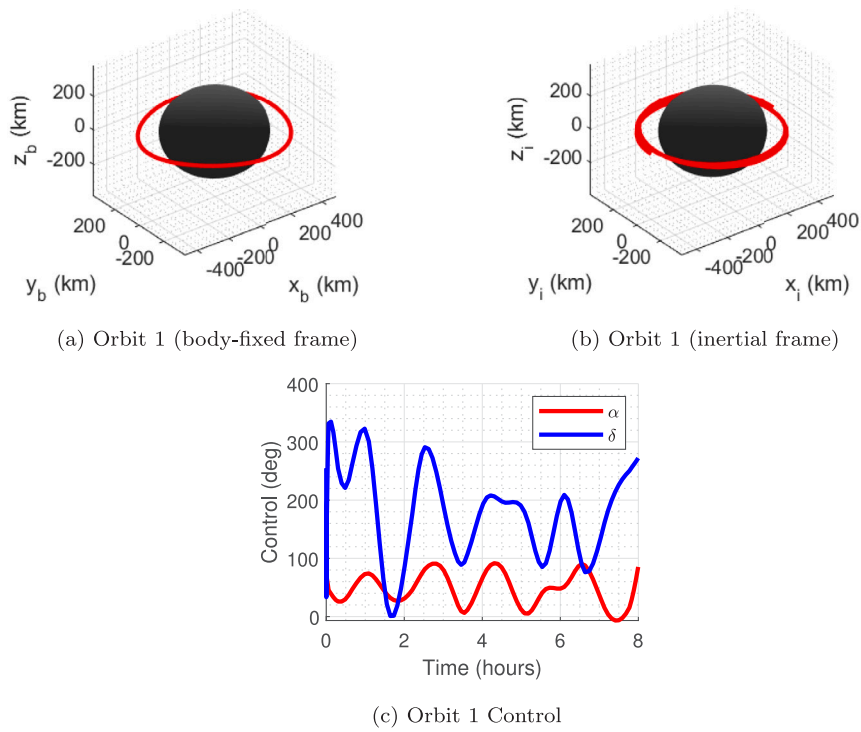
(a) Orbit 1 (body-fixed frame)

(b) Orbit 1 (inertial frame)

(c) Orbit 1 Control

Fig. 13. Deployment orbit 1.

(a) Orbit 2 (body-fixed frame)

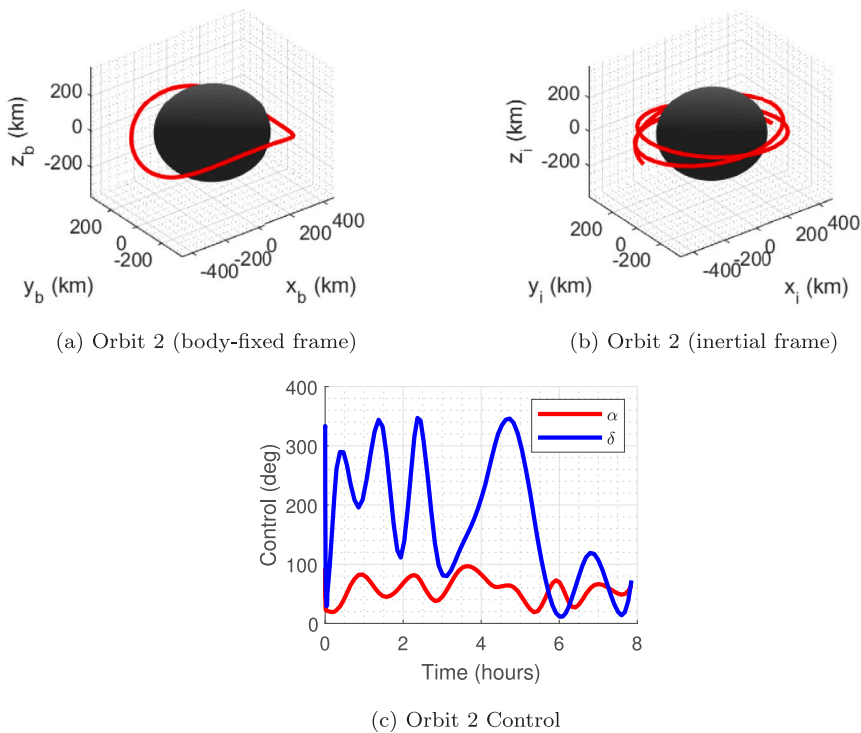(b) Orbit 2 (inertial frame)

(c) Orbit 2 Control

Fig. 14. Deployment orbit 2.

is large and instantaneous. In the first instance, the pre-deployment orbit and control are established. After deployment, the orbit of the sail is maintained in the region of the nominal orbit, converging to a near-equatorial quasi-periodic orbit, by application of TDFC.

5.1. Pre-deployment orbit control

Calculation of the nominal, pre-deployment, orbit of the solar sail is achieved using a GA as described in Section 3. Two deployment orbits
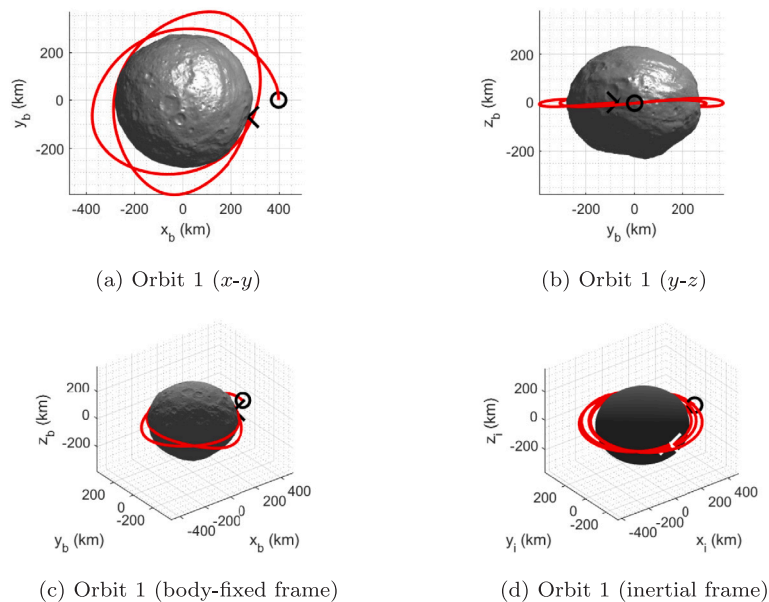
(a) Orbit 1 (*x-y*)

(b) Orbit 1 (*y-z*)

(c) Orbit 1 (body-fixed frame)

(d) Orbit 1 (inertial frame)

Fig. 15. Landing trajectories for deployment from orbit 1.

(a) Orbit 2 (*x-y*)

(b) Orbit 2 (*y-z*)

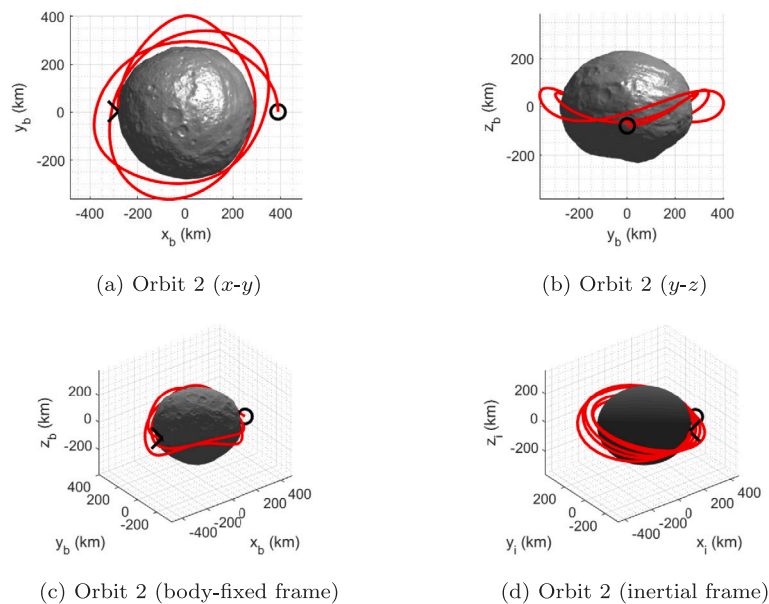(c) Orbit 2 (body-fixed frame)

(d) Orbit 2 (inertial frame)

Fig. 16. Landing trajectories for deployment from orbit 2.

Table 4
Comparison of sailcraft drift from initial hover point for fixed attitude and LQR.

Location	Fixed attitude (km)	LQR a (km)
1	0.3416	0.0072
2	0.1728	0.0082
3	0.1728	0.0071
4	0.1728	0.0080
5	0.1728	0.0079

Table 5
Semi-major axis (SMA) and inclination (INC) of periodic solutions found by GA.

Orbit	SMA (km)	INC (deg)
1	390.81	1.82
2	390.31	14.34

are established using this method: a lower inclination solution (orbit 1) sought by restricting the search for initial state to a small region of the phase space near the equatorial region, and a higher inclination solution (orbit 2) is facilitated by relaxing the constraint on this phase space search. These orbits give a range of potential landing sites for the MASCOT-type lander. Table 5 gives the semi-major axis (SMA) and inclination (INC) of the solutions.

Allowing the GA to select the initial conditions in this way allowed for a solution with the smallest possible objective function value, rather than targeting a specific orbit which resulted in larger objective
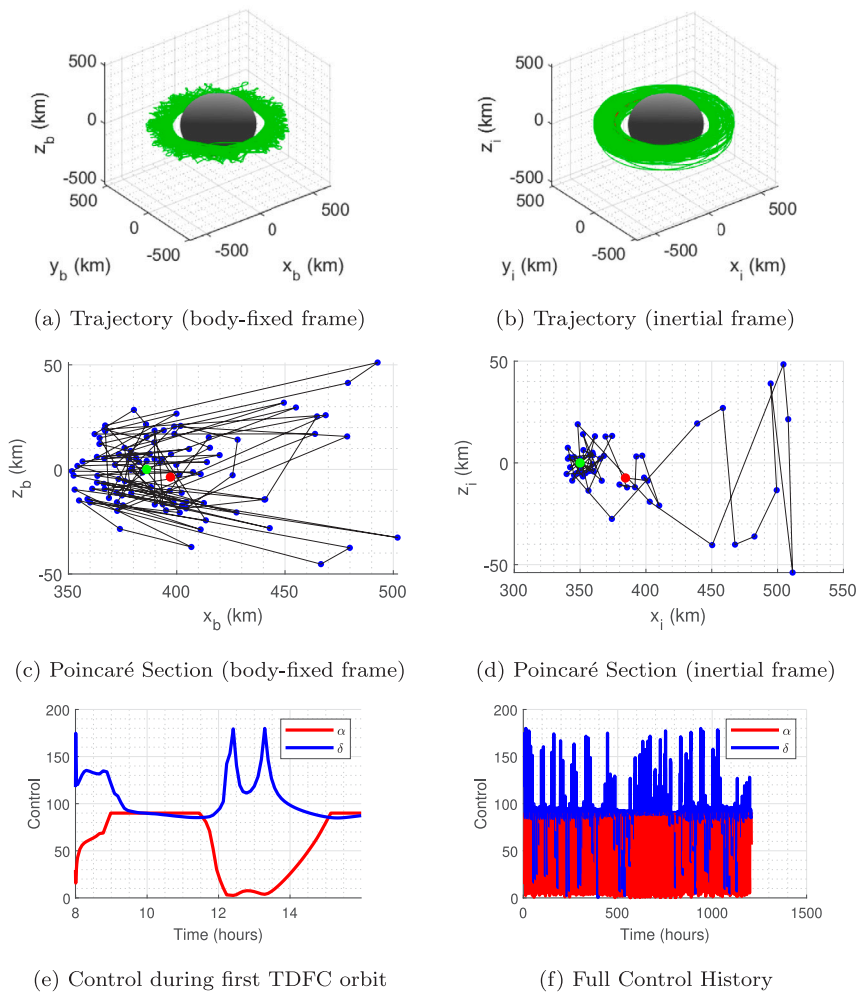
(a) Trajectory (body-fixed frame)

(b) Trajectory (inertial frame)

(c) Poincaré Section (body-fixed frame)

(d) Poincaré Section (inertial frame)

(e) Control during first TDFC orbit

(f) Full Control History

Fig. 17. Post-deployment trajectory and control of the sail using TDFC method after deployment from orbit 1.

function values. If these large errors remained then the sail control would not only have to deal with the instantaneous change in sail acceleration due to lander deployment, but also a large error in the state. Figs. 13 and 14 show orbits 1 and 2 and their control laws.

5.2. Impact conditions for the MASCOT-type lander

Using the deployment orbits obtained in Section 5.1, the landing conditions are now obtained for the MASCOT-type lander and their trajectories are shown in Figs. 15 and 16 for deployment orbits 1 and 2 respectively. As with Section 4.2, the polyhedron shape model is applied to ensure accurate dynamics very close to, and on, the surface. The numerical values for the landing conditions are given in Table 6. It should be emphasised here that the impact conditions were not an objective of this work and are simply presented here for completeness.

From deployment orbit 1, the lander makes a number of close approaches to the surface before the final impact. In the inertial frame, the trajectory describes an orbit under perturbation from a non-spherical body, with rotation of the apse line, until the approach to periapsis bring the lander into contact with the surface. The lander trajectory from deployment orbit 2 shows the same behaviour but the time to impact is extended given the higher inclination initial condition.

5.3. Post-deployment orbit control

When the sailcraft completes one full revolution of the nominal orbit, the lander is released, resulting in an instantaneous increase in

Table 6
Impact conditions for MASCOT-type lander.

	Orbit 1	Orbit 2
Deployment Δv	[0, −5, 0] m/s	[0, −5, 0] m/s
Impact velocity	190.03 m/s	190.86 m/s
Impact latitude	−0.25°	−1.22°
Impact longitude	−14.37°	179.46°
Time to impact	9.53 h	12.63 h

a_c. In order to control the sail such that it converges to a periodic orbit, TDFC is applied. This method is chosen as a proven method of stabilising an unstable periodic orbit [33].

For the TDFC, the matrices **Q** and **R** will be weighted such that the solution favours periodicity over control effort. In order to analyse the convergence of the method, a section of the phase space in the $x - z$ plane will be taken which shows the location where the trajectory intersects that plane on each orbit. For an orbit to be periodic, the final state must converge to the same point in the state space as the initial state [68]. However, for the purposes of illustration, only the positional convergence is shown in the $x - z$ plane in subsequent figures.

Fig. 17 shows the results for correction after deployment from pre-deployment orbit 1. The Poincaré sections in Fig. 17 show that the orbit converges in the inertial frame to a near-equatorial orbit.

Deployment orbit 2 is shown in Fig. 18. Here, the results similarly appear to converge to a planar orbit, though the method takes considerably longer to do so, given the higher starting inclination.
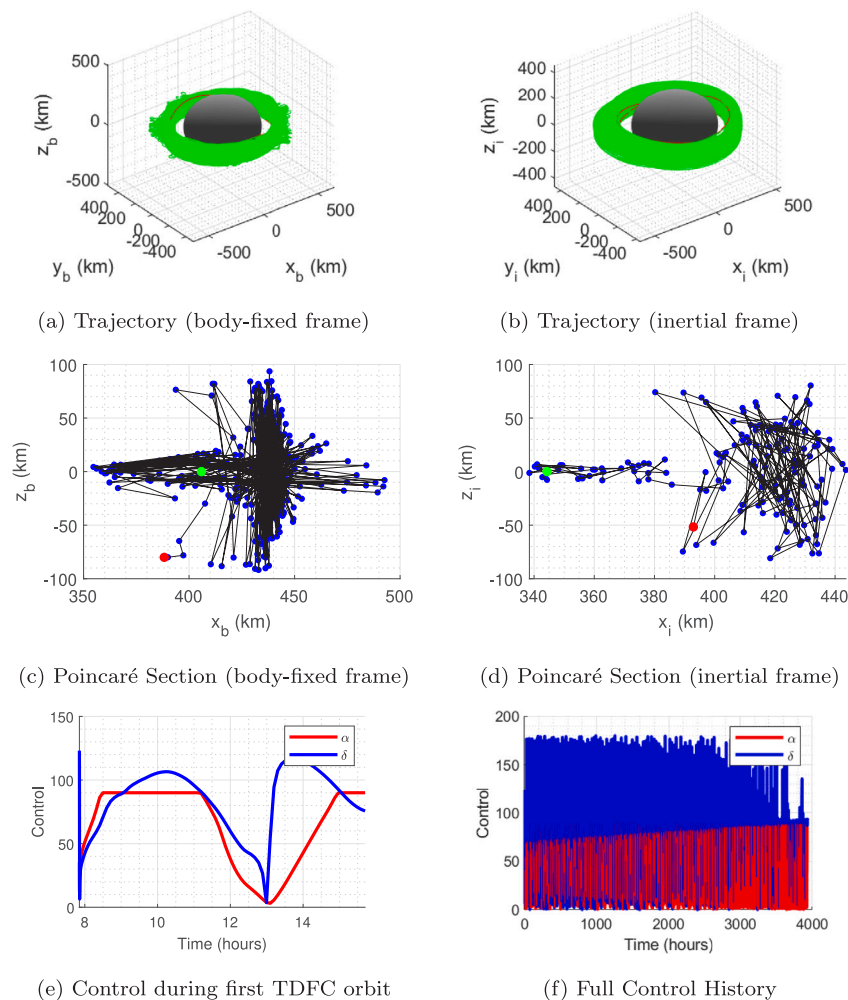
(a) Trajectory (body-fixed frame)

(b) Trajectory (inertial frame)

(c) Poincaré Section (body-fixed frame)

(d) Poincaré Section (inertial frame)

(e) Control during first TDFC orbit

(f) Full Control History

Fig. 18. Post-deployment trajectory and control of the sail using TDFC method after deployment from orbit 2.

6. Conclusion

In this paper, the problem of controlling a solar sail on a stable hover/orbit after the deployment of a series of small probes, or a single large lander, has been addressed. The problem is characterised by an instantaneous change in the sail acceleration and system dynamics at the point of separation of each probe/lander.

In the deployment of a series of small ChipSat probes, the sail was able to successfully hold a position close to the original deployment point. However, the far higher effort required by the sail to maintain the LQR control did not produce results which were of such an improvement over maintaining a fixed sail attitude to warrant their recommendation for a real-world scenario. Five distinct deployment locations were tested and the method was successful in each case. It was found that the deployment location which trailed the asteroid rotation was not able to deploy any of its probes to the asteroid surface, but these probes could support science cases while orbiting.

In the deployment of the larger MASCOT-type lander, two nominal pre-deployment orbits were first established by a GA. Following the completion of the nominal orbit, the lander was deployed and the sail maintained its orbit in the region of the nominal orbit before converging to a near-equatorial orbit using Time-Delay Feedback Control (TDFC). This method was successful for both deployment orbits, though deployment from orbit 2 required far longer to converge to the final planar orbit.

This paper has shown that it is possible for a sail to successfully be controlled after the deployment of small probes and larger landers. This

fills an important gap in the available literature on solar sail missions to asteroids.

Declaration of competing interest

The authors declare the following financial interests/personal relationships which may be considered as potential competing interests: Colin McInnes is supported by the Royal Academy of Engineering under the Chair in Emerging Technologies scheme. Iain Moore is supported by the Engineering and Physical Sciences Research Council (EPSRC) grant number 2126307.

There are no additional interests to declare.

Funding sources

CM is supported by the Royal Academy of Engineering under the Chair in Emerging Technologies scheme. IM is supported by the Engineering and Physical Sciences Research Council (EPSRC) grant number 2126307.

References

[1] D.S. Lauretta, S.S. Balram-Knutson, E. Beshore, W.V. Boynton, C.D. d'Aubigny, D.N. DellaGiustina, H.L. Enos, D.R. Golish, C.W. Hergenrother, E.S. Howell, C.A. Bennett, E.T. Morton, M.C. Nolan, B. Rizk, H.L. Roper, A.E. Bartels, B.J. Bos, J.P. Dworkin, D.E. Highsmith, D.A. Lorenz, L.F. Lim, R. Mink, M.C. Moreau, J.A. Nuth, D.C. Reuter, A.A. Simon, E.B. Bierhaus, B.H. Bryan, R. Ballouz, O.S. Barnouin, R.P. Binzel, W.F. Bottke, V.E. Hamilton, K.J. Walsh, S.R. Chesley, P.R.

Christensen, B.E. Clark, H.C. Connolly, M.K. Crombie, M.G. Daly, J.P. Emery, T.J. McCoy, J.W. McMahon, D.J. Scheeres, S. Messenger, K. Nakamura-Messenger, K. Righter, S.A. Sandford, OSIRIS-REx: Sample return from asteroid (101955) bennu, Space Sci. Rev. 212 (1–2) (2017) 925–984, http://dx.doi.org/10.1007/s11214-017-0405-1.

[2] A.F. Cheng, A.S. Rivkin, P. Michel, J. Atchison, O. Barnouin, L. Benner, N.L. Chabot, C. Ernst, E.G. Fahnestock, M. Kueppers, P. Pravec, E. Rainey, D.C. Richardson, A.M. Stickle, C. Thomas, AIDA DART asteroid deflection test: Planetary defense and science objectives, Planet. Space Sci. 157 (2018) 104–115, http://dx.doi.org/10.1016/j.pss.2018.02.015.

[3] D.K. Yeomans, Radio science results during the NEAR-shoemaker spacecraft rendezvous with eros, Science 289 (5487) (2000) 2085–2088, http://dx.doi.org/10.1126/science.289.5487.2085.

[4] M. Yoshikawa, A. Fujiwara, J. Kawaguchi, Hayabusa and its adventure around the tiny asteroid itokawa, Proc. Int. Astron. Union 2 (14) (2007) http://dx.doi.org/10.1017/s174392130701085x.

[5] M. Beckman, K. Berry, B. Sutter, A. May, K. Williams, B.W. Barbee, B. Williams, OSIRIS-REx touch-and-go (TAG) mission design and analysis, in: 36th Annual AAS Guidance and Control Conference, Breckenridge, CO, USA, 2013.

[6] A. Peloni, M. Ceriotti, B. Dachwald, Solar sail trajectory design for a multiple near-Earth asteroid rendezvous mission, J. Guid. Control Dyn. 39 (12) (2016) 2712–2724, http://dx.doi.org/10.2514/1.G000470.

[7] A. Peloni, Solar-sail mission design for multiple near-Earth asteroid rendezvous (Thesis), 2018, URL http://theses.gla.ac.uk/8901/.

[8] A. Peloni, B. Dachwald, M. Ceriotti, Multiple near-Earth asteroid rendezvous mission: solar-sailing options, Adv. Space Res. 62 (8) (2018) 2084–2098, http://dx.doi.org/10.1016/j.asr.2017.10.017.

[9] G. Viavattene, M. Ceriotti, Artificial neural networks for multiple NEA rendezvous missions with continuous thrust, J. Spacecr. Rockets 59 (2) (2022) 574–586, http://dx.doi.org/10.2514/1.a34799.

[10] E. Yong, X. Wang, Trajectory optimization for multiple asteroid rendezvous mission through hybrid propulsion, in: 2021 33rd Chinese Control and Decision Conference (CCDC), IEEE, 2021, http://dx.doi.org/10.1109/ccdc52312.2021.9601440.

[11] M. Ceriotti, G. Viavattene, I. Moore, A. Peloni, C.R. McInnes, J.T. Grundmann, Sailing at the brink – The no-limits of near-/now-term-technology solar sails and SEP spacecraft in (multiple) NEO rendezvous, Adv. Space Res. 67 (9) (2021) 3012–3026, http://dx.doi.org/10.1016/j.asr.2020.10.017.

[12] Y. Takao, O. Mori, M. Matsushita, A.K. Sugihara, Solar electric propulsion by a solar power sail for small spacecraft missions to the outer solar system, Acta Astronaut. 181 (2021) 362–376, http://dx.doi.org/10.1016/j.actaastro.2021.01.020.

[13] D. Miller, J. Englander, R. Linares, Hybrid solar sailing and electric propulsion: a mission concept to comet 45, in: 2021 AAS/AIAA Astrodynamics Specialist Conference, 2021.

[14] M. Leslie, J. Les, K. Pater, C.-R. Julie, F. Andreas, Near-Earth Asteroid (NEA) Scout, SPACE Conferences and Exposition, American Institute of Aeronautics and Astronautics, 2014, http://dx.doi.org/10.2514/6.2014-4435.

[15] D.J. Scheeres, Orbit mechanics about asteroids and comets, J. Guid. Control Dyn. 35 (3) (2012) 987–997, http://dx.doi.org/10.2514/1.57247.

[16] I. Moore, M. Ceriotti, Solar sails for perturbation relief: Application to asteroids, Adv. Space Res. 67 (9) (2021) 3027–3044, http://dx.doi.org/10.1016/j.asr.2020.08.014.

[17] V. Szebehely, The Theory of Orbits, Academic Press, 1967.

[18] M. Hénon, New families of periodic orbits in hill's problem of three bodies, Celestial Mech. Dynam. Astronom. 85 (3) (2003) 223–246, http://dx.doi.org/10.1023/a:1022518422926.

[19] M. Giancotti, S. Campagnola, Y. Tsuda, J. Kawaguchi, Families of periodic orbits in Hill's problem with solar radiation pressure: application to Hayabusa 2, Celestial Mech. Dynam. Astronom. 120 (3) (2014) 269–286, http://dx.doi.org/10.1007/s10569-014-9564-5.

[20] D. García Yárnoz, D.J. Scheeres, C.R. McInnes, On the a and g families of orbits in the Hill problem with solar radiation pressure and their application to asteroid orbiters, Celestial Mech. Dynam. Astronom. 121 (4) (2015) 365–384, http://dx.doi.org/10.1007/s10569-015-9604-9.

[21] A. Farrés, À. Jorba, J.-M. Mondelo, B. Villac, Periodic motion for an imperfect solar sail near an asteroid, in: Advances in Solar Sailing, Springer Berlin Heidelberg, 2014, pp. 885–898, http://dx.doi.org/10.1007/978-3-642-34907-253.

[22] A. Farrés, À. Jorba, J.-M. Mondelo, Numerical study of the geometry of the phase space of the Augmented Hill Three-Body problem, Celestial Mech. Dynam. Astronom. 129 (1–2) (2017) 25–55, http://dx.doi.org/10.1007/s10569-017-9762-z.

[23] J. Heiligers, D.J. Scheeres, Solar-sail orbital motion about asteroids and binary asteroid systems, J. Guid. Control Dyn. 41 (9) (2018) 1947–1962, http://dx.doi.org/10.2514/1.g003235.

[24] A. Farrés, S. Soldini, Y. Tsuda, JAXA's trojan asteroids mission: Trajectory design of the solar power sail and its lander, in: International Symposium on Solar Sailing 2017, Kyoto, Japan, 2017.

[25] E. Morrow, D.J. Scheeres, D. Lubin, Solar sail orbit operations at asteroids, J. Spacecr. Rockets 38 (2) (2001) 279–286, http://dx.doi.org/10.2514/2.3682.

[26] J. Bookless, C. McInnes, Control of Lagrange point orbits using solar sail propulsion, Acta Astronaut. 62 (2–3) (2008) 159–176, http://dx.doi.org/10.1016/j.actaastro.2006.12.051.

[27] Y. Jiang, H. Baoyin, J. Li, H. Li, Orbits and manifolds near the equilibrium points around a rotating asteroid, Astrophys. Space Sci. 349 (1) (2013) 83–106, http://dx.doi.org/10.1007/s10509-013-1618-8.

[28] Y. Jiang, H. Baoyin, X. Wang, Y. Yu, H. Li, C. Peng, Z. Zhang, Order and chaos near equilibrium points in the potential of rotating highly irregular-shaped celestial bodies, Nonlinear Dynam. 83 (1–2) (2015) 231–252, http://dx.doi.org/10.1007/s11071-015-2322-8.

[29] Y. Jiang, H. Baoyin, Periodic orbit families in the gravitational field of irregular-shaped bodies, Astron. J. 152 (5) (2016) 137, http://dx.doi.org/10.3847/0004-6256/152/5/137.

[30] Y. Jiang, H. Baoyin, X. Wang, H. Li, Stability and motion around equilibrium points in the rotating plane-symmetric potential field, Results Phys. 10 (2018) 487–497, http://dx.doi.org/10.1016/j.rinp.2018.06.056.

[31] Y. Jiang, H. Baoyin, Periodic orbits related to the equilibrium points in the potential of Irregular-shaped minor celestial bodies, Results Phys. 12 (2019) 368–374, http://dx.doi.org/10.1016/j.rinp.2018.11.049.

[32] D. Scheeres, The effect of C22 on orbit energy and angular momentum, Celestial Mech. Dynam. Astronom. 73 (1/4) (1999) 339–348, http://dx.doi.org/10.1023/a:1008384021964.

[33] J.D. Biggs, C.R. McInnes, Time-delayed feedback control in astrodynamics, J. Guid. Control Dyn. 32 (6) (2009) 1804–1811.

[34] F. Scholten, F. Preusker, S. Elgner, K.-D. Matz, R. Jaumann, J. Biele, D. Hercik, H.-U. Auster, M. Hamm, M. Grott, C. Grimm, T.-M. Ho, A. Koncz, N. Schmitz, F. Trauthan, S. Kameda, S. Sugita, R. Honda, T. Morota, E. Tatsumi, Y. Cho, K. Yoshioka, H. Sawada, Y. Yokota, N. Sakatani, M. Hayakawa, M. Matsuoka, M. Yamada, T. Kouyama, H. Suzuki, C. Honda, K. Ogawa, The descent and bouncing path of the Hayabusa2 lander MASCOT at asteroid (162173) Ryugu, Astron. Astrophys. 632 (2019) L3, http://dx.doi.org/10.1051/0004-6361/201936757.

[35] S. Tardivel, The Deployment of Scientific Packages to Asteroid Surfaces (Ph.D. thesis), University of Colorado, 2014, URL https://tel.archives-ouvertes.fr/tel-01062674.

[36] F. Thuillet, Y. Zhang, P. Michel, J. Biele, S. Kameda, S. Sugita, E. Tatsumi, S.R. Schwartz, R.-L. Ballouz, Numerical modeling of lander interaction with a low-gravity asteroid regolith surface, Astron. Astrophys. 648 (2021) A56, http://dx.doi.org/10.1051/0004-6361/201936128.

[37] Y. Tsuda, T. Saiki, F. Terui, S. Nakazawa, M. Yoshikawa, S. ichiro Watanabe, Hayabusa2 mission status: Landing, roving and cratering on asteroid ryugu, Acta Astronaut. 171 (2020) 42–54, http://dx.doi.org/10.1016/j.actaastro.2020.02.035.

[38] S. Van wal, R.G. Reid, D.J. Scheeres, Simulation of nonspherical asteroid landers: Contact modeling and shape effects on bouncing, J. Spacecr. Rockets 57 (1) (2020) 109–130, http://dx.doi.org/10.2514/1.A34573.

[39] T. Timmons, G. Bailet, J. Beeley, C. McInnes, Mars atmospheric characterization with a ChipSat swarm, J. Spacecr. Rockets (2021) 1–8, http://dx.doi.org/10.2514/1.a34970.

[40] T.-M. Ho, V. Baturkin, C. Grimm, J.T. Grundmann, C. Hobbie, E. Ksenik, C. Lange, K. Sasaki, M. Schlotterer, M. Talapina, N. Termtanasombat, E. Wejmo, L. Witte, M. Wrasmann, G. Wübbels, J. Rößler, C. Ziach, R. Findlay, J. Biele, C. Krause, S. Ulamec, M. Lange, O. Mierheim, R. Lichtenheldt, M. Maier, J. Reill, H.-J. Sedlmayr, P. Bousquet, A. Bellion, O. Bompis, C. Cenac-Morthe, M. Deleuze, S. Fredon, E. Jurado, E. Canalias, R. Jaumann, J.-P. Bibring, K.H. Glassmeier, D. Hercik, M. Grott, L. Celotti, F. Cordero, J. Hendrikse, T. Okada, MASCOT–the mobile asteroid surface scout onboard the Hayabusa2 mission, Space Sci. Rev. 208 (1–4) (2016) 339–374, http://dx.doi.org/10.1007/s11214-016-0251-6.

[41] L. Niccolai, M. Bassetto, A.A. Quarta, G. Mengali, A review of Smart Dust architecture, dynamics, and mission applications, Prog. Aerosp. Sci. 106 (2019) 1–14, http://dx.doi.org/10.1016/j.paerosci.2019.01.003.

[42] A.A. Quarta, G. Mengali, L. Niccolai, Smart dust option for geomagnetic tail exploration, Astrodynamics 3 (3) (2019) 217–230, http://dx.doi.org/10.1007/s42064-019-0048-3.

[43] M. Ceriotti, C.R. McInnes, Natural and sail-displaced doubly-symmetric Lagrange point orbits for polar coverage, Celestial Mech. Dynam. Astronom. 114 (1–2) (2012) 151–180, http://dx.doi.org/10.1007/s10569-012-9422-2.

[44] M. Ceriotti, J.P. Sanchez, Control of asteroid retrieval trajectories to libration point orbits, Acta Astronaut. 126 (2016) 342–353, http://dx.doi.org/10.1016/j.actaastro.2016.03.037.

[45] E. Morrow, D. Scheeres, D. Lubin, Solar sail orbit operations at asteroids, in: Astrodynamics Specialist Conference, American Institute of Aeronautics and Astronautics, 2000, http://dx.doi.org/10.2514/6.2000-4420.

[46] G. Frieger, 3D asteroid catalogue, 2013-2020, Accessed: 2022-02-18. https://3d-asteroids.space/asteroids/.

[47] T. Williams, M. Abate, Capabilities of furlable solar sails for asteroid proximity operations, J. Spacecr. Rockets 46 (5) (2009) 967–975, http://dx.doi.org/10.2514/1.30355.

[48] C.R. McInnes, Solar Sailing: Technology, Dynamics and Mission Applications, Springer-Praxis, Chichester, 1999.

[49] X. Huang, X. Zeng, C. Circi, G. Vulpetti, D. Qiao, Analysis of the solar sail deformation based on the point cloud method, Adv. Space Res. 67 (9) (2021) 2613–2627, http://dx.doi.org/10.1016/j.asr.2020.05.008.

[50] D. Vallado, Fundamentals of Astrodynamics, fourth ed, Space Technology Library, 2013.

[51] C.R. McInnes, A.J.C. McDonald, J.F.L. Simmons, E.W. MacDonald, Solar sail parking in restricted three-body systems, J. Guid. Control Dyn. 17 (2) (1994) 399–406, http://dx.doi.org/10.2514/3.21211.

[52] W.S. Koon, J.E. Marsden, S.D. Ross, M. Lo, D.J. Scheeres, Geometric mechanics and the dynamics of asteroid pairs, Ann. New York Acad. Sci. 1017 (1) (2004) 11–38, http://dx.doi.org/10.1196/annals.1311.002.

[53] D.J. Scheeres, Orbital Motion in Strongly Perturbed Environments, Springer, 2012.

[54] S. Cicalò, D.J. Scheeres, Averaged rotational dynamics of an asteroid in tumbling rotation under the YORP torque, Celestial Mech. Dynam. Astronom. 106 (4) (2010) 301–337, http://dx.doi.org/10.1007/s10569-009-9249-7.

[55] F. Preusker, F. Scholten, K.-D. Matz, T. Roatsch, R. Jaumann, C. Raymond, C. Russell, Dawn FC2 Derived Vesta DTM SPG V1.0, Technical Report, NASA Planetary Data System, 2016.

[56] A. Rossi, F. Marzari, P. Farinella, Orbital evolution around irregular bodies, Earth Planets Space 51 (1999) 1173–1180.

[57] A. Viale, C. McInnes, M. Ceriotti, Dynamics of a nonrigid orbital siphon at a near-earth asteroid, J. Guid. Control Dyn. (2020) 1–15, http://dx.doi.org/10.2514/1.g004894.

[58] R.F. Stengel, Optimal Control and Estimation, Dover Publications Inc, 1994.

[59] J.D. Biggs, C.R. McInnes, An optimal gains matrix for time-delayed feedback control, in: 2nd IFAC Conference on TheControl of Chaos, 2009.

[60] R. Hevner, W. Holemans, J. Puig-Suari, R. Twiggs, An Advanced Standard for CubeSat. in: Proceedings of the 25th Annual AIAA/USU Conference on Small Satellites, Logan, UT, USA, 2011.

[61] B. Dachwald, H. Boehnhardt, U. Broj, U.R.M.E. Geppert, J.-T. Grundmann, W. Seboldt, P. Seefeldt, P. Spietz, L. Johnson, E. Kührt, S. Mottola, M. Macdonald, C.R. McInnes, M. Vasile, R. Reinhard, Gossamer roadmap technology reference study for a multiple neo rendezvous mission, in: M. Macdonald (Ed.), Advances in Solar Sailing, Springer Berlin Heidelberg, Berlin, Heidelberg, 2014, pp. 211–226, http://dx.doi.org/10.1007/978-3-642-34907-215.

[62] M.E. Leipold, O. Wagner, Mercury sun-synchronous polar orbits using solar sail propulsion, J. Guid. Control Dyn. 19 (6) (1996) 1337–1341, http://dx.doi.org/10.2514/3.21791.

[63] W.K. Wilkie, J.E. Warren, L.G. Horta, K.H. Lyle, J.-N. Juang, J.D. Littell, R.G. Bryant, M.W. Thomson, P.E. Walkemeyer, D.V. Guerrant, D.A. Lawrence, S.C. Gibbs, E.H. Dowell, A.F. Heaton, Heliogyro solar sail research at NASA, in: Advances in Solar Sailing, Springer Berlin Heidelberg, 2014, pp. 631–650, http://dx.doi.org/10.1007/978-3-642-34907-239.

[64] G. Mengali, A.A. Quarta, Solar sail near-optimal circular transfers with plane change, J. Guid. Control Dyn. 32 (2) (2009) 456–463, http://dx.doi.org/10.2514/1.38079.

[65] M. Macdonald, C. McGrath, T. Appourchaux, B. Dachwald, W. Finsterle, L. Gizon, P.C. Liewer, C.R. McInnes, G. Mengali, W. Seboldt, T. Sekii, S.K. Solanki, M. Velli, R.F. Wimmer-Schweingruber, P. Spietz, R. Reinhard, Gossamer roadmap technology reference study for a solar polar mission, in: Advances in Solar Sailing, Springer Berlin Heidelberg, 2014, pp. 243–257, http://dx.doi.org/10.1007/978-3-642-34907-217.

[66] M. Ceriotti, C.R. McInnes, B.L. Diedrich, The pole-sitter mission concept: An overview of recent developments and possible future applications, in: 62nd International Astronautical Congress, Cape Town, South Africa, 2011.

[67] Z. Liu, M. Fang, L. Shi, Z. Chen, J. Li, H. Long, W. Zhu, Numerical and experimental analyses of component failure risk in a mobile phone under drop test, IEEE Trans. Compon., Packag. Manuf. Technol. 12 (1) (2022) 69–79, http://dx.doi.org/10.1109/tcpmt.2021.3134102.

[68] W.E. Wiesel, Modern Astrodynamics, second ed., Aphelion, 2010.